



Multifrequency corner states in acoustic second-order topological insulatorsWeibai Li , Guoxing Lu, and Xiaodong Huang ^{*}*School of Engineering, Swinburne University of Technology, Hawthorn, Victoria 3122, Australia*

(Received 25 October 2023; revised 21 February 2024; accepted 22 February 2024; published 13 March 2024)

Second-order topological insulators possess unique boundary states beyond the conventional bulk-boundary correspondence, which provides opportunities for multidimensional wave manipulation in electronic and acoustic systems. This paper develops an acoustic second-order topological insulator by sonic crystals, hosting multiple corner states at different frequency ranges within one complete bandgap. The topologically protected multifrequency corner states provide robust control of acoustic waves with good immunity against defects. The one-dimensional sound propagation and zero-dimensional sound localization at different frequencies are experimentally observed. We also find these multifrequency corner states are susceptible to the bandgap size of sonic crystals, which could be systematically tuned through topology optimization. The reported results expand the boundaries of constructing second-order topological insulators and exploring multifrequency localized wave modes.

DOI: [10.1103/PhysRevB.109.104308](https://doi.org/10.1103/PhysRevB.109.104308)**I. INTRODUCTION**

Sonic crystals (SnCs) are artificial materials created by periodically allocating scatters to induce energy bands. The exceptional properties of the bandgap in SnCs, where phonons or waves cannot transmit through the crystal structure, have been widely explored [1–4]. The realization of SnCs in different forms offers a promising platform for wave manipulation [5–8], e.g., waveguide [9], vibration isolator [10], unidirectional sound propagation [11], and imaging [12].

The discovery of topological insulators [13–15], initially proposed in electromagnetic systems and expanded to mechanical [16–19] and acoustic [20–22] fields, has brought renewed attention to the band properties of photonic and phononic crystals. Topological insulators (TIs) insulate waves in the “bulk” but host topologically protected states at the interfaces, which provides a promising route to superconductors [14,23]. In the conventional TIs based on the quantum spin Hall effect [15,24] or the quantum valley Hall effect [25,26], the topological edge states are gapless. Comparably, second-order topological insulators in three dimensions can host gapped surface states and gapless hinge states [27,28]. Increasing interests have been focused on the photonics [29], and outstanding achievements have been recorded, such as TIs with topologically protected edge states [30–32], corner states [33–36], quantized Weyl centers [37], and chiral modes [38]. In the acoustic system, SnCs are the ideal medium for studying topological phases of matter due to their macroscopic structures that are easy to fabricate. Acoustic TIs have been investigated in gradient one-dimensional (1D) SnCs for sound trapping [39], two-dimensional (2D) cases by the tight-binding model [40],

kagome lattice [41], sandwichlike heterostructure [42], arbitrary corner structures [43] and optimized structures [44], and three-dimensional (3D) cases with multidimensional sound propagation [45–48].

This paper reports a second-order TI constructed by trivial and nontrivial maraca-shaped SnCs created by topology optimization. The TI possesses gapped bulk-edge bands hosting 0D corner states and 1D edge states at the interface between nontrivial and trivial SnCs. Significantly, the specially designed second-order TI exhibits multifrequency corner modes, which can be expected within an enlarged bandgap but has rarely been reported in the acoustic system. For example, different types of corner states in one structure were presented by rotating triangle scatters [43] or tuning the coupling in the tight-binding model [49]. Different from the existing investigation relying on physical intuition and being limited to simple geometries, this paper paves the way for multifrequency corner states by designing the structures in an artificial intelligence manner. These multifrequency corner states are topologically protected and robust against defects. These results are verified by numerical simulation and experiment with good agreement. Further, the multifrequency corner states are susceptible to the bandgap size and may merge into the bulk or the edge states as the bandgap size decreases. An intelligent design approach, topology optimization, is proposed to systematically tune the bandgap size.

II. RESULTS**A. Topological insulator by sonic crystals**

As shown in Fig. 1(a), the 2D lattice consists of two material phases (solid in black and air in white) with C_{4v} symmetry. UC1 is obtained by our topology optimization method [50,51], which formulates the problem mathematically and seeks the optimal solid/air distribution

^{*}xhuang@swin.edu.au

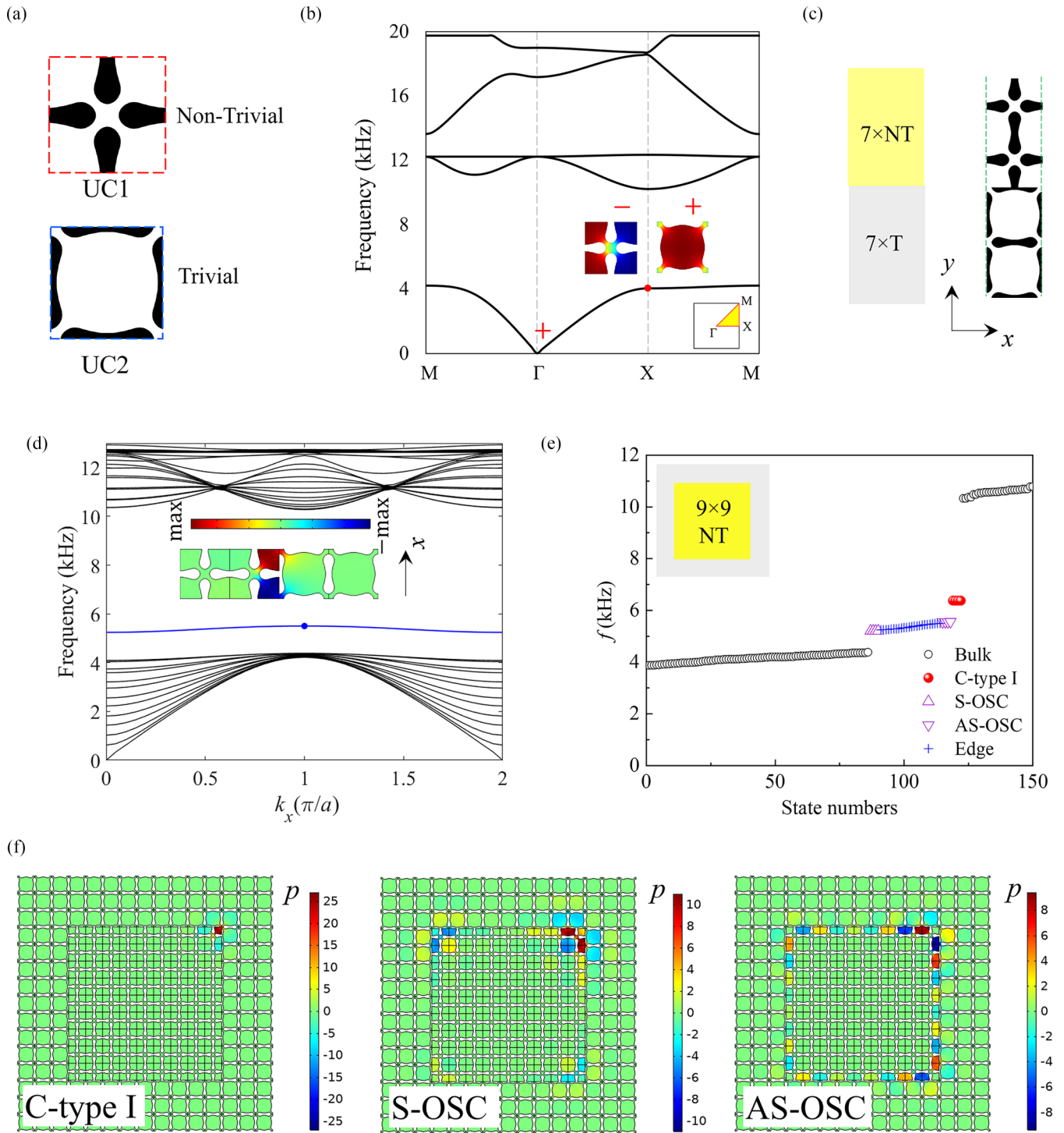


FIG. 1. Second-order topological properties in SnCs. (a) The unit cells obtained by topology optimization. The black areas denote the solid structures, and thereafter figures. (b) Band diagram of the unit cells. The topological index can be indicated by the parities of eigenstates, which preserve at Γ but reverse at X . “+” denotes even parity, while “-” denotes odd parity. (c) Schematic of the bar-shaped supercell. (d) The projected band diagram. The blue line indicates the gapped edge states, and the inset shows the pressure distribution when $k_x = \pi/a$. (e) Calculated eigenspectra of the topological insulator whose configuration is shown in the inset. (f) Sound pressure distribution for the corner state and the off-site corner states.

within the lattice so that the size of the bandgap is maximized. UC2 is the counterpart by translating the periodic UC1 with half of the lattice constant, $a = 18.9$ mm, along both the horizontal and the vertical directions. The bulk band

dispersion of the SnCs along boundaries of the irreducible Brillouin zone is calculated in Fig. 1(b), showing a complete bandgap in the frequency range of 4.21–10.21 kHz. The topological properties of the unit cells can be determined by

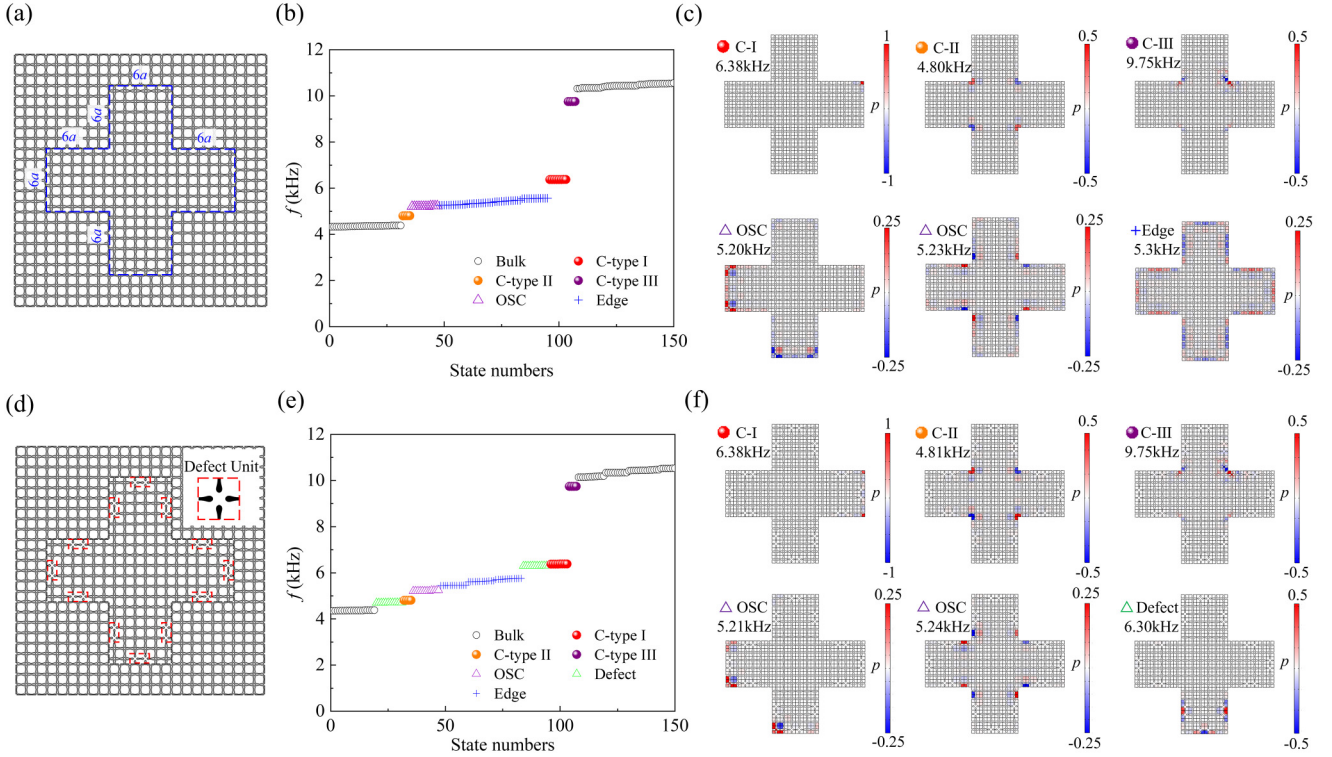


FIG. 2. Numerical simulation of topological states. (a) and (d) Images of the TI without and with defects. The blue dashed lines indicate the interface between trivial and nontrivial SnCs. (b) and (e) Calculated eigenspectra corresponding to the models. The red dots indicate the type I corner states at convex corners. The orange and purple dots denote the type II and type III corner states at the concave corners, respectively. (c) and (f) Simulated sound pressure profiles of multifrequency corner states, off-site corner states, the edge state, and the defect state, respectively. The color bars are normalized by the maximum sound pressure value at the C-type I corner states.

the bulk polarization [52,53] $\mathbf{P} = (P_x, P_y)$:

$$P_i = \frac{1}{2} \left(\sum_n q_i^n \bmod 2 \right), \quad (1)$$

$$(-1)^{q_i^n} = \frac{\eta_n(X_i)}{\eta_n(\Gamma)}. \quad (2)$$

The summation is taken over all the bands below the target bandgap. $i = x, y$ in 2D cases, and \mathbf{X}_i is the high symmetric point X [$\mathbf{k} = (a/\pi, 0)$] and Y [$\mathbf{k} = (0, a/\pi)$]. $\mathbf{k} = (k_x, k_y)$ is the Bloch wave vector along the boundary of the first irreducible Brillouin zone. η_n represents the parity of the n th Bloch eigenstate at the high-symmetry points in the Brillouin zone, where an even parity and an odd parity are defined as positive (“+”) and negative (“−”), respectively. Due to the mirror symmetries, the parities of Y are the same as X . Then, a trivial topological phase can be indicated by $\mathbf{P}=(0,0)$ from Eq. (1), while $\mathbf{P}=(1/2,1/2)$ is for the nontrivial topological phase. In order words, a trivial/nontrivial sonic crystal has an even/odd number of pairs of opposite parities at $X(Y)$ and Γ .

It can be theoretically proved that the above translation between UC1 and UC2 will reverse the bulk polarization of eigenstates at the high-symmetry point X but preserve it at point Γ . Therefore, UC1 and UC2 have opposite topological properties essential for a TI based on the generalized Su-Schrieffer-Heeger (SSH) model [54–56]. To reveal the gapped edge band, we have calculated a ribbon configuration by COMSOL MULTIPHYSICS, as shown in Fig. 1(c). The Floquet-Bloch

periodic boundary is applied to the left and right borders. The top and bottom ends employ the plane wave radiation boundary, which is a class of nonreflecting boundary conditions assuming that there is an outgoing plane wave. The projected band diagram is presented in Fig. 1(d), where an edge band emerges at 5.25–5.5 kHz. The inset shows the pressure distribution of an edge mode, $k_x = \pi/a$ and $f = 5.5$ kHz, with sound waves propagating through the interface between the nontrivial and trivial units. As shown in Fig. 1(e), we calculate the eigenspectra for a second-order topological insulator, which comprises 9×9 nontrivial units surrounded by three layers of trivial units. Figure 1(f) illustrates the sound pressure distribution for three different corner states: the conventional type I corner states with sound waves highly concentrated at the corners, the symmetric off-site corner state, and the anti-symmetric off-site corner state, which localize sound waves on edges near the corner but not exactly at the cornermost sites [49]. Distinguished from the C-type I showing an obvious gap to the edge and bulk states, the presence of such off-site corner states is always close to either end of edge states.

B. Multifrequency corner states

To explore the existence of multifrequency corner states within the wide bandgap range, we consider the corner structure depicted in Fig. 2(a). The nontrivial SnCs form 90° (convex) and 270° (concave) bent angles on the interface with

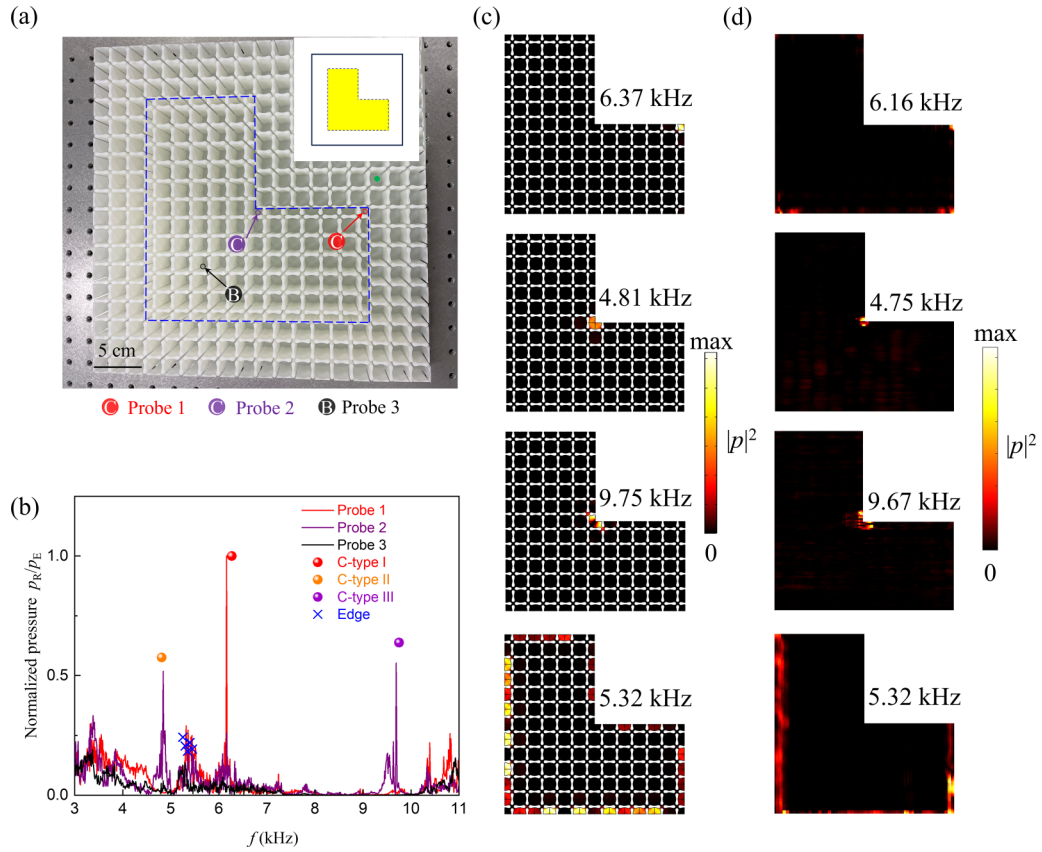


FIG. 3. (a) Photograph of the fabricated sample and probe locations. The inset demonstrates the sound pressure scanning field within the yellow area. (b) Measured frequency response. (c) Simulated and (d) measured sound profiles at selected frequencies.

trivial SnCs. Besides the C-type I and off-site corner states, the calculated eigenspectra in Fig. 2(b) show additional type II and type III corner states locating at the lower- and higher-frequency edge-bulk gaps, respectively. The simulated field profiles corresponding to specific eigenstates are illustrated in Fig. 2(c), where the trivial SnCs are peeled off to display a close look at topological interfaces. Compared to the C-type I states with sound localization at the convex corners, the C-type II and C-type III states have the highest field values at the concave corners. The C-type II state exhibits a symmetric field profile with respect to the angle bisector of each corner, while it is antisymmetric in the C-type III state. To confirm that the three types of corner states are topologically protected, we introduce defects into the TI by replacing some units on the interface, as shown in Fig. 2(d). The defect unit, framed by red dashed lines, is an eroded structure considering manufacturing errors. The corresponding eigenspectra in Fig. 2(e) shows that the imperfect model also holds the three types of corner states at 4.81, 6.38, and 9.75 kHz, respectively, supporting the robust control of acoustic wave in the TI. Interestingly, the defect modes with the sound pressure concentrated around the defect units arise near the C-type I and C-type II but not near the type III states.

To experimentally realize the multifrequency sound localization, we fabricate a sample with photosensitive resin via 3D stereolithography printing. As shown in Fig. 3(a), this sample contains six corners with intersection angles of 90° and 270° . The bottom of the sample is sealed by a 6-mm-thick

slab, and the top was covered by an acrylic sheet. Probes 1 and 2 are installed through the cover sheet at the convex and concave corners, respectively. Probe 3 is placed within the bulk of the nontrivial part. The excitation source is the sine wave signal generated by the sound card of a BSWA MC3242 data collector and played by a broadband headphone placed in one cavity of the sample. High sensitivity free-field microphones MPA416 and the NI 9322 data acquisition card are used to measure the sound pressures. The sound transmission spectra ranging from 3 to 11 kHz are probed and plotted in Fig. 3(b). It is difficult to control the pressure magnitude of the sound source during the experiment. Therefore, the ratio of measured response pressure to that of the excitation source, $|p_R|/|p_E|$, is scaled by the peak value at 6.16 kHz to provide a qualitative comparison with numerical results. The calculated topological states normalized by the maximum value at 6.27 kHz are denoted by red, orange, purple, and blue markers in Fig. 3(b). The experiment measurement agrees well with the numerical calculation, and the sharp peaks at about 4.8, 6.16, and 9.69 kHz indicate the existence of multifrequency corner modes. In the frequency range of edge bands (5.2–5.6 kHz), sound transports along the edges are detected with lower pressures than the corner states, while extremely low signal levels are collected in the stop band between 6.3 and 9.3 kHz.

Then, we measure the pressure profile of multiple selected frequencies near the peaks, 4.75, 5.32, 6.16, and 9.67, to observe the sound localization at corners and propagation through edges. The fabricated sample is fixed on a two-axis

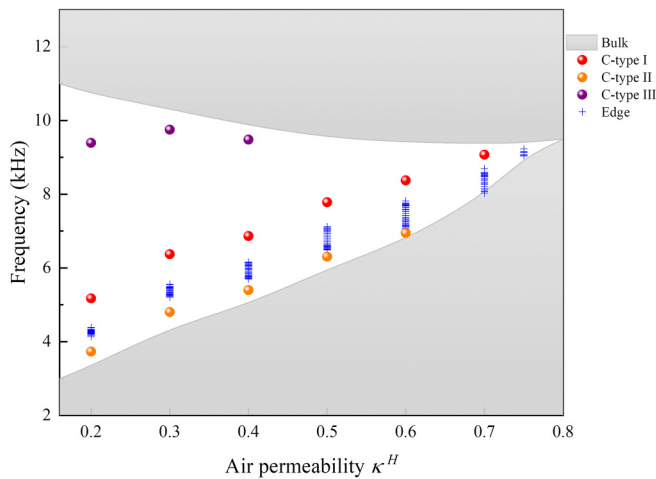


FIG. 4. Gap-size dependent corner states.

motorized stage whose moving step length is 2 mm. The microphone is installed in the top cover, leaving a gap of about 1 mm between the surface and the sample that can move smoothly. The scan area is the whole domain within the blue dashed lines in Fig. 3(a). The simulated and measured sound intensity distributions are shown in Figs. 3(c) and 3(d), respectively. Overall, the experimental measurements agree well with the simulation results. Sound localization can be found at different frequencies and locations, and the pressure peaks decay rapidly into the bulk.

Nevertheless, an SSH-based TI cannot guarantee the emergence of the type II and type III corner states, which are susceptible to the SnC bandgap size. Therefore, we tune the bandgap size of SnCs by air connectivity constraint via topology optimization [50]. The air connectivity, κ^H , takes values between 10^{-3} and 1, where $\kappa^H = 1$ for a unit cell full of air and $\kappa^H = 10^{-3}$ for the solid to block the propagation of sound waves. The increasing value denotes better air connectivity within the unit cell but results in a smaller bulk bandgap. In Fig. 4, we calculate the eigenstates of the corresponding structures. Multifrequency corner states emerge in the

edge-bulk gaps. For $\kappa^H = 0.2 - 0.7$, the type I corner states (marked by red nodes) are perfectly isolated from the edge and bulk states. However, the type II and type III states for concave corners (marked by orange and purple nodes) are sensitive to the gap size. As the bulk bandgap narrows, the type II corner state with a lower frequency moves towards the edge. It merges into the edge due to the lower bulk-edge gap closing at $\kappa^H = 0.7$. On the other hand, the type III corner state merges into the bulk when $\kappa^H = 0.5$, even without the closure of the upper bulk-edge gap. Therefore, the appearance of type II and type III corner states are highly related to the topologies of the SnCs.

III. CONCLUSIONS

In conclusion, we present an optimized acoustic second-order TI featuring multifrequency corner states. Compared to the TIs possessing multiple corner states within a narrow bandgap, the corner structure in this paper hosts three types of corner states occurring in significantly separate excitation frequencies. Moreover, the multifrequency corner states allow for trapping acoustic waves at convex or concave corners with different field distributions. This feature can be potentially applied in energy harvesting and wave filtering. Numerical simulation and experiments reveal the 1D propagation mode and verify that the corner modes robustly localize the wave energy at the convex corners (type I) and concave corners (types II and III) with different wave frequencies. The type II and III states at concave corners are susceptible to the bandgap size that can be switched on or off by tuning the air connectivity of SnCs in the optimization design process. Our work provides a systematic design approach for constructing second-order TIs to manipulate the propagation of acoustic wave among bulk, edge, and corner modes under multiple frequencies.

ACKNOWLEDGMENT

This work was supported by the Australian Research Council (Grant No. DP210103523).

- [1] M. S. Kushwaha, P. Halevi, L. Dobrzynski, and B. Djafari-Rouhani, Acoustic band structure of periodic elastic composites, *Phys. Rev. Lett.* **71**, 2022 (1993).
- [2] V. Laude, *Phononic Crystals: Artificial Crystals for Sonic, Acoustic, and Elastic Waves*, De Gruyter Studies in Mathematical Physics (De Gruyter, Berlin, 2015).
- [3] V. Romero-García, in *Acoustic Waves in Periodic Structures, Metamaterials, and Porous Media: From Fundamentals to Industrial Applications*, edited by N. Jiménez, O. Umnova, and J.-P. Groby (Springer International Publishing, Cham, 2021), p. 65.
- [4] T. Miyashita, Sonic crystals and sonic wave-guides, *Meas. Sci. Technol.* **16**, R47 (2005).
- [5] M.-H. Lu, L. Feng, and Y.-F. Chen, Phononic crystals and acoustic metamaterials, *Mater. Today* **12**, 34 (2009).
- [6] I. R. H. Olsson and I. El-Kady, Microfabricated phononic crystal devices and applications, *Meas. Sci. Technol.* **20**, 012002 (2009).
- [7] W. Li, F. Meng, Y. Chen, Y.-F. Li, and X. Huang, Topology Optimization of Photonic and Phononic Crystals and Metamaterials: A Review, *Adv. Theory Simul.* **2**, 1900017 (2019).
- [8] Y. Pennec, J. O. Vasseur, B. Djafari-Rouhani, L. Dobrzyński, and P. A. Deymier, Two-dimensional phononic crystals: Examples and applications, *Surf. Sci. Rep.* **65**, 229 (2010).
- [9] V. Laude, Principles and properties of phononic crystal waveguides, *APL Mater.* **9**, 080701 (2021).
- [10] V. Zega, L. Pertoldi, T. Zandrini, R. Osellame, C. Comi, and A. Corigliano, Microstructured phononic crystal isolates from ultrasonic mechanical vibrations, *Appl. Sci.* **12**, 2499 (2022).
- [11] X.-F. Li, X. Ni, L. Feng, M.-H. Lu, C. He, and Y.-F. Chen, Tunable unidirectional sound propagation through a sonic-crystal-based acoustic diode, *Phys. Rev. Lett.* **106**, 084301 (2011).
- [12] C. Qiu, X. Zhang, and Z. Liu, Far-field imaging of acoustic waves by a two-dimensional sonic crystal, *Phys. Rev. B* **71**, 054302 (2005).

- [13] C. L. Kane and E. J. Mele, Quantum spin Hall effect in graphene, *Phys. Rev. Lett.* **95**, 226801 (2005).
- [14] J. E. Moore, The birth of topological insulators, *Nature (London)* **464**, 194 (2010).
- [15] X.-L. Qi and S.-C. Zhang, Topological insulators and superconductors, *Rev. Mod. Phys.* **83**, 1057 (2011).
- [16] H. Fan, B. Xia, L. Tong, S. Zheng, and D. Yu, Elastic higher-order topological insulator with topologically protected corner states, *Phys. Rev. Lett.* **122**, 204301 (2019).
- [17] S. Li, D. Zhao, H. Niu, X. Zhu, and J. Zang, Observation of elastic topological states in soft materials, *Nat. Commun.* **9**, 1370 (2018).
- [18] S.-Y. Huo, J.-J. Chen, H.-B. Huang, and G.-L. Huang, Simultaneous multi-band valley-protected topological edge states of shear vertical wave in two-dimensional phononic crystals with veins, *Sci. Rep.* **7**, 10335 (2017).
- [19] Z. Du, J. Luo, Z. Xu, Z. Jiang, X. Ding, T. Cui, and X. Guo, Higher-order topological insulators by ML-enhanced topology optimization, *Int. J. Mech. Sci.* **255**, 108441 (2023).
- [20] A. B. Khanikaev, R. Fleury, S. H. Mousavi, and A. Alù, Topologically robust sound propagation in an angular-momentum-biased graphene-like resonator lattice, *Nat. Commun.* **6**, 8260 (2015).
- [21] Z. Yang, F. Gao, X. Shi, X. Lin, Z. Gao, Y. Chong, and B. Zhang, Topological acoustics, *Phys. Rev. Lett.* **114**, 114301 (2015).
- [22] Z. Zhang, Q. Wei, Y. Cheng, T. Zhang, D. Wu, and X. Liu, Topological creation of acoustic pseudospin multipoles in a flow-free symmetry-broken metamaterial lattice, *Phys. Rev. Lett.* **118**, 084303 (2017).
- [23] A. Rashidi, R. Kealhofer, A. C. Lygo, V. Huang, and S. Stemmer, Induced superconductivity in the two-dimensional topological insulator phase of cadmium arsenide, *APL Mater.* **11**, 041117 (2023).
- [24] B. A. Bernevig, T. L. Hughes, and S.-C. Zhang, Quantum spin Hall effect and topological phase transition in HgTe quantum wells, *Science* **314**, 1757 (2006).
- [25] D. Xiao, W. Yao, and Q. Niu, Valley-contrasting physics in graphene: Magnetic moment and topological transport, *Phys. Rev. Lett.* **99**, 236809 (2007).
- [26] K. F. Mak, K. L. McGill, J. Park, and P. L. McEuen, The valley Hall effect in MoS₂ transistors, *Science* **344**, 1489 (2014).
- [27] L. Trifunovic and P. W. Brouwer, Higher-order topological band structures, *Phys. Status Solidi B* **258**, 2000090 (2021).
- [28] L. Fu, Topological crystalline insulators, *Phys. Rev. Lett.* **106**, 106802 (2011).
- [29] H. Wang, S. K. Gupta, B. Xie, and M.-H. Lu, Photonic crystals and topological photonics, *Front. Optoelectron.* **13**, 50 (2020).
- [30] K. Kawabata, K. Shiozaki, and M. Ueda, Anomalous helical edge states in a non-Hermitian Chern insulator, *Phys. Rev. B* **98**, 165148 (2018).
- [31] Z. Song, Z. Fang, and C. Fang, ($d - 2$)-Dimensional edge states of rotation symmetry protected topological states, *Phys. Rev. Lett.* **119**, 246402 (2017).
- [32] S. Mukherjee, A. Spracklen, M. Valiente, E. Andersson, P. Öhberg, N. Goldman, and R. R. Thomson, Experimental observation of anomalous topological edge modes in a slowly driven photonic lattice, *Nat. Commun.* **8**, 13918 (2017).
- [33] S. Mittal, V. V. Orre, G. Zhu, M. A. Gorkach, A. Poddubny, and M. Hafezi, Photonic quadrupole topological phases, *Nat. Photon.* **13**, 692 (2019).
- [34] B.-Y. Xie, H.-F. Wang, H.-X. Wang, X.-Y. Zhu, J.-H. Jiang, M.-H. Lu, and Y.-F. Chen, Second-order photonic topological insulator with corner states, *Phys. Rev. B* **98**, 205147 (2018).
- [35] X.-D. Chen, W.-M. Deng, F.-L. Shi, F.-L. Zhao, M. Chen, and J.-W. Dong, Direct observation of corner states in second-order topological photonic crystal slabs, *Phys. Rev. Lett.* **122**, 233902 (2019).
- [36] K. Koizumi, H. T. Phan, K. Nishigomi, and K. Wakabayashi, Topological edge and corner states in the biphenylene network, *Phys. Rev. B* **109**, 035431 (2024).
- [37] W. A. Benalcazar, T. Li, and T. L. Hughes, Quantization of fractional corner charge in C_n -symmetric higher-order topological crystalline insulators, *Phys. Rev. B* **99**, 245151 (2019).
- [38] F. Schindler, A. M. Cook, M. G. Vergniory, Z. Wang, S. S. P. Parkin, B. A. Bernevig, and T. Neupert, Higher-order topological insulators, *Sci. Adv.* **4**, eaat0346 (2018).
- [39] C. Liu, Z. Zhang, D. Liao, Z. Yue, C. Ma, Y. Cheng, and X. Liu, Rainbow trapping for sound waves in one-dimensional topological insulator, *Appl. Phys. Lett.* **123**, 041701 (2023).
- [40] Z.-G. Chen, C. Xu, R. A. I. Jaldali, J. Mei, and Y. Wu, Corner states in a second-order acoustic topological insulator as bound states in the continuum, *Phys. Rev. B* **100**, 075120 (2019).
- [41] H. Xue, Y. Yang, F. Gao, Y. Chong, and B. Zhang, Acoustic higher-order topological insulator on a kagome lattice, *Nat. Mater.* **18**, 108 (2019).
- [42] H. Li, Z. Wang, Z. Wang, Z. Liu, X. Zhang, J. Luo, J. Huang, X. Wang, and H. Yang, Experimental observation of the multiple higher-order extensible topological states in acoustic systems, *Phys. Rev. Appl.* **18**, 044050 (2022).
- [43] X. Zhang, L. Liu, M.-H. Lu, and Y.-F. Chen, Valley-selective topological corner states in sonic crystals, *Phys. Rev. Lett.* **126**, 156401 (2021).
- [44] R. E. Christiansen, F. Wang, and O. Sigmund, Topological insulators by topology optimization, *Phys. Rev. Lett.* **122**, 234502 (2019).
- [45] F. Meng, Y. Chen, W. Li, B. Jia, and X. Huang, Realization of multidimensional sound propagation in 3D acoustic higher-order topological insulator, *Appl. Phys. Lett.* **117**, 151903 (2020).
- [46] F. Meng, Z.-K. Lin, W. Li, P. Yan, Y. Zheng, X. Li, J.-H. Jiang, B. Jia, and X. Huang, Observation of emergent Dirac physics at the surfaces of acoustic higher-order topological insulators, *Adv. Sci.* **9**, 2201568 (2022).
- [47] X. Zhang, B.-Y. Xie, H.-F. Wang, X. Xu, Y. Tian, J.-H. Jiang, M.-H. Lu, and Y.-F. Chen, Dimensional hierarchy of higher-order topology in three-dimensional sonic crystals, *Nat. Commun.* **10**, 5331 (2019).
- [48] M. Weiner, X. Ni, M. Li, A. Alù, and A. B. Khanikaev, Demonstration of a third-order hierarchy of topological states in a three-dimensional acoustic metamaterial, *Sci. Adv.* **6**, eaay4166 (2020).
- [49] W. Xiong, S. Wang, Z. Zhang, H. Zhang, Y. Cheng, and X. Liu, Observation of multiple off-site corner states induced by next-nearest-neighbor coupling in a sonic crystal, *Phys. Rev. B* **109**, 024305 (2024).

- [50] W. Li, J. Hu, G. Lu, and X. Huang, Topology optimization of acoustic bandgap crystals for topological insulators, *Eng. Comput.* (2024), doi:[10.1007/s00366-023-01936-2](https://doi.org/10.1007/s00366-023-01936-2).
- [51] X. Huang and W. Li, Three-field floating projection topology optimization of continuum structures, *Comput. Methods Appl. Mech. Eng.* **399**, 115444 (2022).
- [52] F. Liu and K. Wakabayashi, Novel topological phase with a zero Berry curvature, *Phys. Rev. Lett.* **118**, 076803 (2017).
- [53] C. Fang, M. J. Gilbert, and B. A. Bernevig, Bulk topological invariants in noninteracting point group symmetric insulators, *Phys. Rev. B* **86**, 115112 (2012).
- [54] W. P. Su, J. R. Schrieffer, and A. J. Heeger, Solitons in polyacetylene, *Phys. Rev. Lett.* **42**, 1698 (1979).
- [55] F. Liu, H.-Y. Deng, and K. Wakabayashi, Topological photonic crystals with zero Berry curvature, *Phys. Rev. B* **97**, 035442 (2018).
- [56] D. Obana, F. Liu, and K. Wakabayashi, Topological edge states in the Su-Schrieffer-Heeger model, *Phys. Rev. B* **100**, 075437 (2019).